Complete thermoelectric benchmarking of individual InSb nanowires by combined micro-Raman and electric transport analysis

Sara Yazji[1,2], Eric Hoffman[1,2], Daniele Ercolani[3], Francesco Rossella[3], Alessandro Pitanti[3], Alessandro Cavalli[1], Stefano Roddaro[3], Gerhard Abstreiter[1,2], Lucia Sorba[3], and Ilaria Zardo[1,4]

[1]*Walter Schottky Institut & Physik Department, Technische Universität München, D-85748 Garching, Germany*

[2]*Institute for Advanced Study, Technische Universität München, D-85748 Garching, Germany*

[3]*NEST, Istituto Nanoscienze-CNR and Scuola Normale Superiore, I-56127 Pisa, Italy*

[4]*Applied Physics, Photonics & Semiconductor Nanophysics, Eindhoven University of Technology, MB 5600 Eindhoven, The Netherlands*

Abstract

Nanowires are ideal nanostructures for exploring the effects of low-dimensionality and thermal conductivity suppression on thermoelectric behavior. However, it is challenging to accurately measure temperature gradients and heat flow in such systems. Here, using combined spatially-resolved Raman spectroscopy and transport measurements, we determine all the thermoelectric properties of single Se-doped InSb nanowires and to quantify the ZT figure of merit. The measured laser-induced heating in the nanowires and the associated electrical response are well-described by a one-dimensional heat equation model. Our results demonstrate that the thermal contact resistances at the source and drain electrodes of the nanowire play a crucial role and cannot be neglected in such mesoscopic devices. The measured thermoelectric parameters of InSb nanowires are compared with those obtained by field-effect transistor Seebeck measurements, obtaining a good agreement.

1. Introduction

High efficiency heat-electricity conversion can have a major impact on energy production and enable new self-powered device applications. , The figure of merit $ZT = \sigma S^2 T/\kappa$ (where σ, S, and κ are the electrical conductivity, the Seebeck coefficient, and the thermal conductivity, respectively) relates the physical properties of a material with its efficiency as power generator or as heat pump. After the predicted enhancement of the ZT value for materials at the nanoscale [Hicks1, Hicks2], a large number of materials with $ZT > 1$ at room temperature were discovered [Majumdar, Heremans], even if a competitive material with $ZT > 3$ has not been developed yet. To the best of our knowledge, the highest reached ZT value is 2.6 at 923 K, realized in SnSe single crystals measured along the b axis of the room-temperature orthorhombic unit cell [Zhao]. In order to give a complete determination of the thermoelectric properties of a material, σ, S and κ need to be measured simultaneously. For systems at the nanoscale, this is very challenging. For nanowires (NWs), κ was often measured using either suspended SiN_x membranes [Roh, Li, Zhou2011] or via local laser heating and Raman spectroscopy [Doerk2010, Soini]. The Seebeck coefficient or the power factor σS^2 can instead be measured using devices with metallic resistive thermometers, designed in several geometries [Zhou2006, Shapira, RodNR2014]. A significant effort has been devoted to engineering measurement platforms that allow a complete determination of the thermoelectric properties of individual NWs. At present, many measurements on NWs have been carried out with suspended resistive thermometers similar to the ones described in reference [Shi2003], which require very complex nanofabrication processes.

Furthermore, an open issue is the determination of the thermal contact resistance R_C between the NW and the thermometers [Shi2012].

In this work, we present a new efficient method for the determination of the thermoelectric properties and figure of merit of single NWs, based on combined spatially-resolved Raman spectroscopy and transport measurements. Our approach is less critical for what concerns the troublesome thermal contact resistances, which can be directly estimated from our measurements and are found to be sizably smaller than in the case of the microheating membranes [Zhou2011a]. In addition, the method is in principle fully compatible with the field-effect control of the carrier density in the nanostructure, which has been recently recognized to be very important in the investigation of fundamental properties of nanostructured thermoelectric materials [RodNL2013]. The temperature gradient ΔT necessary for thermoelectric measurements is provided by the excitation laser, which acts also as thermometer. Raman spectroscopy is indeed used to determine the local temperature enhancement along the NW. Transport and Raman measurements, together with a simple 1D heating model, allow the determination of the parameters needed for the calculation of the ZT together with the estimate of the thermal contact resistance R_C.

We apply this novel method to individual Se-doped InSb NWs, which among III-V semiconductors are expected to be the most promising candidates for thermoelectric application: InSb NWs with diameter of ~10 nm are for instance expected to have ZT ~ 6 at 300 K [Mingo]. In general, InSb is a narrow band gap semiconductor (0.18 eV) with small effective mass at room temperature and high carrier mobility. In the past, thermoelectric properties of bulk InSb have been widely investigated. The thermal conductivity of bulk InSb has been measured in the broad temperature range from 2 K to 773 K [Stuckes, Bowers, Mielczarek, Bush, Holland, Bhandari, Kosarev] and the room temperature thermal conductivity was found to be ~17 W/mK [Bush, Holland, Nakwaski]. The complete thermoelectric properties investigation of intrinsic bulk InSb has been done between 100°C and 500°C, and the average value of the ZT parameter was found to be $0.42*10^{-3}K^{-1}$ [Bowers]. More recently for a Te-doped InSb single crystal a ZT value of 0.6 at 637 K was measured [Yamaguchi].

The thermoelectric figure of merit of single Sb-enriched n-type InSb NWs has been recently measured as a function of growth parameters, with a suspended microdevice [Zhou]. A large suppression of the thermal conductivity with respect to bulk InSb was found (~3 times smaller), but the measured Seebeck coefficient was smaller respect to the value measured for single crystal [Yamaguchi], resulting in a lower ZT (between 0.002 and 0.006 at room temperature). Here, we obtained values of ZT for Se-doped InSb NWs ranging from 0.014 to 0.025 at room temperature, which is slightly larger than previous founding in InSb NWs, though still lower that the ZT of Te-doped bulk single crystals.

2. Method, devices and experimental details

We developed a new method for the investigation the thermoelectric figure of merit of nanostructured materials, consisting in combined spatially-resolved Raman spectroscopy and transport measurements. In the frame of this work we determine the figure of merit of several single Se-doped InSb NWs.

Au-assisted Se-doped InSb NWs are grown by chemical beam epitaxy on InAs (111)B substrates, with a InSb length of ~4.5 μm and diameters in the range ~50-200 nm. Morphology, structure and growth protocol of the NWs are presented in detail in the Supplementary Information (SI1).

In order to estimate the thermoelectric figure of merit $ZT = S^2\sigma T/\kappa$ of a system, we need to determine its thermal conductivity κ, Seebeck coefficient S, and electrical conductivity σ. In the past, the thermal conductivity of semiconductor NWs was already estimated using laser heating and Raman spectroscopy [Doerk2010, Soini]. By employing combined spatially resolved Raman spectroscopy and transport measurements we are able to measure S and σ with a simple method, as it will be discussed in the following.

The excitation laser employed for Raman spectroscopy is moved along the NW heating it locally, and thus generating the necessary temperature gradient ΔT between the ends of the NW, which is suspended between two metallic stripes that act as heat sinks. In addition, two top contacts are deposited at the NW ends, allowing electrical measurements. At each position of the laser, the Raman spectrum and the current-voltage (I-V) characteristic are recorded simultaneously. Through the I-V curves, σ as well as the thermovoltage (*i.e.* the open-circuit voltage V_{OC}) - and therefore the Seebeck coefficient - can be evaluated . The temperature profile along the NW is determined by Raman spectroscopy using the linear relation between the shift $\Delta\nu$ of the TO phonon frequency and the increase in temperature caused by the laser heating [Carles, Costa]. The scans along the NWs are performed for several laser powers, *i.e.* several temperature profiles are measured.

A schematic of the device employed for our measurements is shown in Figure 1. Several parallel gold stripes with 100 nm thickness (10/90 nm of Ti/Au), 2 µm width, and ~2 µm separation were fabricated *via* optical lithography and metal evaporation on a SiO_2/Si substrate. The InSb NWs were dropcasted on the device and the wires suspended between two gold stripes were identified using optical imaging. Subsequently, the top contacts were fabricated using electron beam lithography and evaporating 10/120 nm of Ti/Au. A scanning electron micrograph (SEM) of a typical investigated InSb NW is shown in figure 2(a). The gold stripes were connected to the electronic setup. The bias was supplied using a dc voltage source and the current was measured via a low-noise current preamplifier.

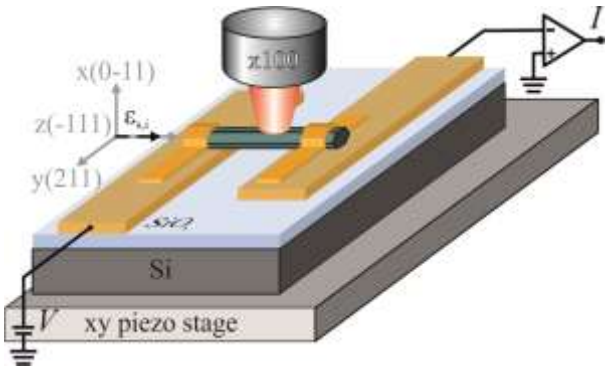

Figure1: Schematic of the device and of the scattering geometry used for Raman spectroscopy. The InSb nanowire is suspended between two gold stripes evaporated on a SiO_2/Si substrate, and clamped with two top contacts. A voltage is applied at one end of the nanowire, and the current is measured through a low-noise current amplifier. The Raman scattering configuration is also shown, together with the nanowire geometry. The entire device is located on a *xy* piezo stage.

We used the 676.4 nm line (E_L = 1.83 eV) of a tunable Ar^+-Kr^+ laser, focused through a 100x objective with 0.95 numerical aperture, both as excitation energy for Raman spectroscopy and as local heater of the NW. The Gaussian spot size of the laser has a full width at half maximum (FWHM) of ~840 nm. For each NW we selected the laser power in order to avoid local Sb segregation and structural modification of the NW (see SI2) [Liarokapis, Yazji]. The Raman spectra were collected by an XY Dilor triple spectrometer equipped with a Si multichannel charged couple detector, with a resolution of ~1cm^{-1}. The device was placed on a *xy* piezo stage with a precision of 10 nm, which allowed spatially resolved measurements.

In Table I we report the geometrical characteristics of the NWs investigated with the combined Raman spectroscopy and electrical measurements method.

Nanowire	Diameter (nm)	$L_{S,D}$ (μm)	L thermal (μm)
A	145	2.200	1.560
B	150	2.240	1.880
C	150	2.340	1.870
D	195	2.410	1.940

Table I: Summary of the geometrical parameters of the investigated Se-doped InSb NWs, as estimated from SEM images. $L_{S,D}$ indicated the part of the InSb NW between source and drain contact. L thermal is instead the suspended part of the NW over the separation between the lower gold stripes. Both lengths are shown in Figure 2 (a).

To cross-check the results obtained by the combined Raman and open-circuit transport measurements, we have also used field-effect transistor measurements for the determination of the thermoelectric parameters of individual n-doped InSb NWs. To this aim, we have fabricated devices implementing a buried heating scheme that allows driving both a large thermal bias (up to temperature gradients of ~8 K/μm along the NW) and a strong field-effect modulation of electrical conductance on the nanostructure. With respect to the previous method, this approach suffers from the fact that it does not allow the estimation of the thermal conductance. However, on the other hand, it is much versatile because it allows the precise mapping of the evolution of the Seebeck coefficient S as a function of the gate-controlled electrical conductivity σ in the desired temperature range. In our case we have addressed the thermoelectric response of the NWs for over 40 temperature values between 86 K and 360 K (see SI3 for the full dataset presentation and analysis). Large thermovoltage values in excess of 1 mV have been induced in devices comprising a single InSb NW as the active element, and these values were modulated by a field effect. From the back-gate dependence of the conductance we can extract the standard field effect electron mobility $\mu_{e,FE}$ value.. However, this value is known to be underestimated since it is strongly affected by surface states and gate hysteresis effects. To bypass this problem we provided an independent estimate of the "Seebeck" electron mobility $\mu_{e,S}$ based on the dependence of the S *vs* σ curves on electron scattering times (see SI4) [RodNL2013].

3. Laser heating and Raman spectroscopy

The combination of laser heating and Raman spectroscopy has already proven to be effective for the determination of the thermal conductivity of NWs [Doerk2010, Soini]. The measurement principle is based on the determination of the local temperature from the shift of the phonon frequencies registered *via* Raman spectroscopy. The excitation laser itself produces a local rise in temperature, which reflects on the creation of a temperature gradient ΔT between the ends of the NW. ΔT is evaluated by fitting the temperature profile with a 1D heat equation which includes laser heating. We observe a difference in the magnitude of the temperature gradient at the NW ends which we attribute to a difference in the thermal contact resistances.

We measured the Raman spectra of InSb NWs in backscattering configuration, and in the geometry illustrated in Figure 1. The excitation polarization ε_i and detection polarization ε_s are selected parallel to the NW axis z, corresponding to the [-111] direction. In this geometry, the Raman spectra present the transversal optical mode (TO) at ~179 cm^{-1}, which is the allowed mode from the selection rules, and the forbidden longitudinal LO mode at 210 cm^{-1} with lower intensity [Zardo]. The shift $\Delta\nu$ of the TO mode caused by laser heating was used to determine the local temperature rise as a function of the laser position x_L. We assumed the same linear coefficient between $\Delta\nu$ and local temperature rise (with

respect to ambient temperature) T_{rise} measured for bulk InSb, *i.e.* $\Delta\nu/T_{rise} = 0.016$ cm^{-1}/K [Carles, Costa], in analogy to the experimental observation on Si NWs [Doerk2009]. A typical temperature profile obtained is shown in figure 2(b) (open black diamonds) for the NW in figure 2(a) at a fixed laser power (135 μW, corresponding to a power density of 24 kW/cm^2) together with the spatially resolved Raman shifts (filled blue diamonds). The spectra were collected every 250 nm along the NW. We collected two spectra integrating 180 seconds per spectrum for each laser position which were averaged.

It has to be noted that the temperature deduced by Raman spectroscopy is associated with the thermal vibrations of the crystal lattice (lattice temperature). At room temperature, phonons and electrons are well coupled. On the time scale of our measurements, the two systems are in thermal equilibrium and Raman spectroscopy is also a valid electron thermometer.

4. Measurements, 1D heating model and data analysis

The novelty of the measurement technique developed in this work with respect to Ref. [Soini] is the possibility to determine on the same NW their transport properties and then to quantify the figure of merit of single InSb NWs.

To access the Seebeck coefficient $S = V_{th}/\Delta T$, we need to measure the thermovoltage V_{th} of our system. One possible way is to measure directly the open-circuit voltage V_{OC} at the NW ends via a high impedance voltage amplifier, while heating the NW with the laser. However, in this way we do not have simultaneous information on the changes of the electrical conductivity. We therefore decided to extract V_{OC} from I-V characteristics recorded varying the position of the laser on the NW. Therefore we applied an external bias V and recorded the current I with a low noise current amplifier. The applied bias was kept always below 10 mV to avoid additional Joule heating. Without applying a thermal gradient (laser off), for good ohmic contacts we expect $V(I = 0) = 0$. When the laser is on, $\Delta T \neq 0$ and the open circuit thermovoltage appears, as well as the close circuit thermocurrent I_{SC}. From the linear fit to the I-V curves, we can extract $V_{OC,}$ $I_{SC,}$ and the conductance G as a function of the laser position along the NW. At every laser position, we averaged six I-V curves. As an example, the position dependent I-V curves and Raman spectra relative to Figure 2 are shown in the Supplementary Information (SI5, Figure S6). For comparison, we show the spatially resolved thermovoltages measured both from the I-V curves and with open circuit conditions in the SI6 (Figure S7).

In figure 2(c) a typical trend of V_{OC}, I_{SC}, and G is shown for one of the Se-doped InSb NW (D) at a fixed laser power. The laser position was varied moving from the source to the drain contact along the same NW shown in figure 2(a), collecting simultaneously the Raman spectra from which the temperature profile in figure 2(b) was extracted. V_{OC} (I_{SC}) first shows an increase (decrease) then a decrease (increase) as a function of laser position, approaching zero approximately when the local temperature rise reaches the maximum, and changing sign going ahead along the NW. This is exactly in agreement with our expectations: the temperature difference at the contacts ΔT is higher when the laser is close to one of the contacts and goes to zero in the middle of the NW - where the local temperature rise is maximum - reversing its sign throughout the other contact. The local temperature profile generated from the laser heating reflects also on the behavior of the conductance G. It has minima at the NW ends (lowest temperature) and a maximum approximately at the NW center (highest temperature). Similar behavior of G with temperature was obtained by independent electrical measurements (see SI7 Figure S8).

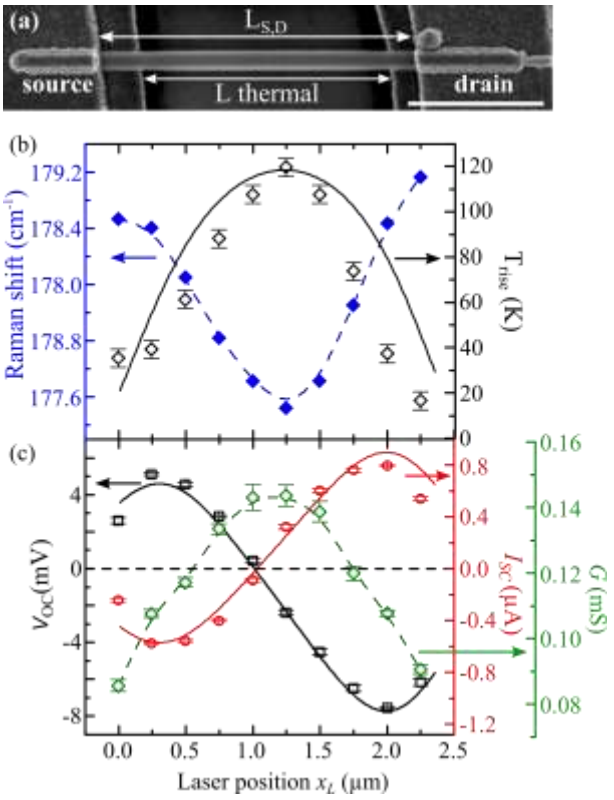

Figure 2: (a) Scanning electron micrograph of one of the investigated Se-doped NW, with 150 nm diameter (NW C). The NW is suspended between two gold contacts; the two top contacts are visible. $L_{S,D}$ and the thermal length (L thermal) are indicated with arrows. The scale bar is 1 μm. (b) Shift of the TO frequency (filled bue diamonds) and local temperature rise (open black diamonds) as a function of the laser position along the NW, for 135 μW laser power. (c) Values of the open circuit voltage V_{OC} (open black squares), closed circuit current I_{SC} (open red circles), and conductance G (open green diamonds) extracted from the I-V characteristic curves measured as a function of the laser position. The I-V measurements were collected simultaneously to the Raman spectra relative to (b). Solid lines are fit of the 1D heating model to the experimental data. Dashed lines are guides to the eyes.

Temperature data obtained by Raman spectroscopy together with V_{OC} and I_{SC} data were analyzed using a 1D heating model including Gaussian heating source, as described in the following.

Because the electrical contacts have a much larger mass and much higher thermal conductivity than the NW, we treat the contacts as ideal heat sinks that remain at room temperature T_{RT}. The NW temperature, T_{NW}, increases under illumination by the Raman excitation laser positioned at x_L. The laser Gaussian beam profile dissipates its power non-uniformly along the NW generating a local temperature rise $T(x) = T_{NW}(x) - T_{RT}$. At the same time, heat is dissipated by convection from the NW into the surrounding atmosphere at a rate $\kappa_{air}T(x)$, where κ_{air} is the thermal conductance to air per unit length. Altogether, the 1D heat equation including laser heating and convective cooling is

$$\kappa A \frac{d^2T(x)}{dx^2} = \kappa_{air}T(x) - \frac{P_{abs}}{w}\sqrt{\frac{2}{\pi}}\,\mathrm{Exp}\left[-\frac{2(x-x_L)^2}{w^2}\right],$$

where the rightmost term describes the Gaussian laser beam profile centered at x_L and having a beam waist w. The Gaussian is normalized so that the total integrated power is $P_{abs} = aP$, where a is the NW absorption coefficient and P is the laser power. A is the NW´s cross sectional area.

This second-order differential equation requires two boundary conditions. These boundary conditions are related to the contact resistances at the source/drain as discussed in the SI8.

The NW cross sectional area A and the laser beam waist is calculated from the measured FWHM , while the absorption coefficient P_{abs} was estimated via *ab initio* finite difference simulations performed with MEEP software [Oskooi, Soini]. In Figure 2(b) and 2(c) we show as solid lines an example of the fit to the experimental data obtained for one NW using global fit procedure, namely using the same parameters for all the data set and changing only the laser power. The agreement between data point and the model is quite good.

From the fitting of the Raman temperature rise with the 1D heat equation, the values of the temperature difference between the contacts ΔT has been calculated (see SI8), and therefore we could estimate the Seebeck coefficient. The experimental data were also fitted via individual fitting procedure, which showed consistent results. More details about the fitting procedures are reported in the SI8.

In Figure 3 we show the obtained electrical conductivities σ (a), Seebeck coefficients S (b), thermal conductivities κ (c), and the thermal contact resistances $R^{C}_{S,D}$ (d) for the investigated Se-doped InSb NWs. Each NW is indicated with a different symbol. In panel (a) we show with the filled symbols the maximum electrical conductivities extrapolated from the power dependence of the σ (σ_{max}), that were calculated from the position dependent measurements (see SI8 and Figure S11 for the details). With the half-filled symbols we indicate the dark electrical conductivities as measured in absence of laser excitation. The dashed line indicates the σ value measured for Te-doped InSb bulk single crystal. The shaded grey area indicates the range of electrical conductivities measured for Sb-doped InSb NWs from Reference [Zhou]. The values of σ_{max} are not significantly different from the previously measurements on Sb-doped NWs [Zhou].

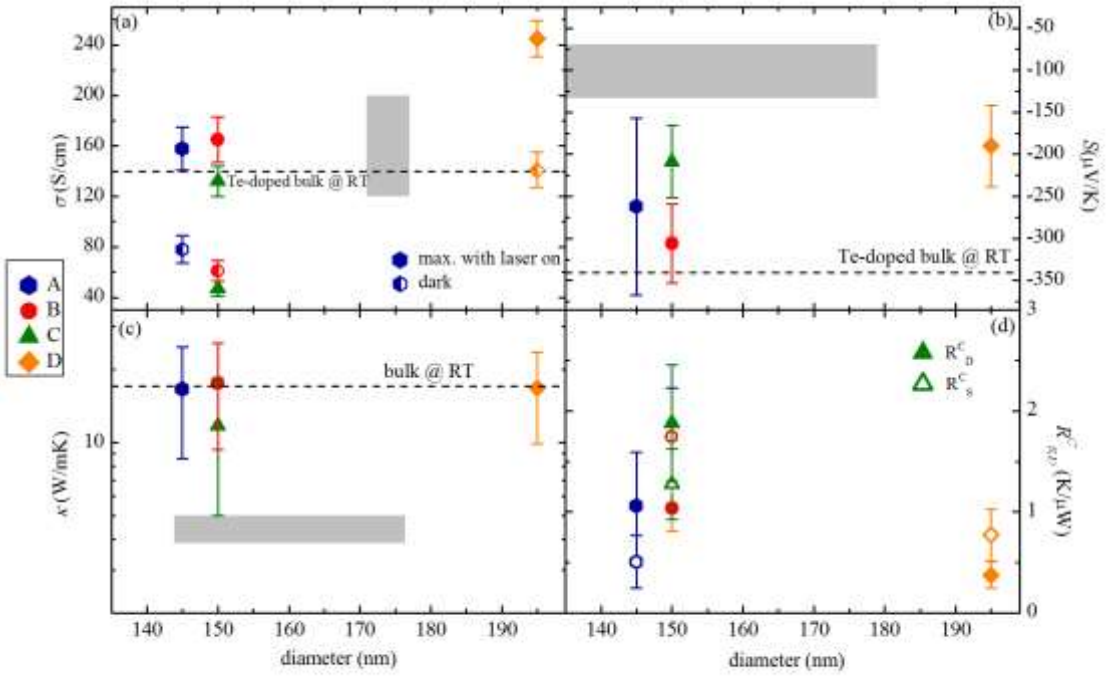

Figure 3: (a) The electrical conductivity σ of different investigated single Se-doped InSb NWs plotted as a function of their diameter. Filled symbols indicate the maximum σ extrapolated from the power dependence of σ (σ_{max}), that were calculated from the position dependent measurements. The half-filled symbols indicate the dark electrical conductivities derived by transport measurements. (b) The Seebeck coefficient S of the different investigated Se-doped InSb NWs plotted as a function of their diameter. (c) The thermal conductivity κ of the different investigated Se-doped InSb NWs plotted

as a function of their diameter. (d) The thermal contact resistances for source (S, empty symbols) and drain (D, filled symbols) as a function of NW diameter. The values of the different parameters obtained from the same NW are represented always with the same symbol. The bulk values of the different parameters are marked as dashed lines for Te-doped single crystal in (a) and (b) [Yamaguchi], and intrinsic bulk in (c) [Bowers]. The range of values obtained by NWs from Ref. [Zhou] is marked as shadowed grey areas.

We observe negative Seebeck coefficients, as expected for n-type semiconductors. The *S* absolute value of Se-doped InSb NWs is generally larger than what reported so far for InSb NWs [Zhou], but in average lower than the Seebeck coefficient measured for Te-doped InSb bulk.

The thermal conductivities (Figure 3(c)), are comparable with the intrinsic InSb bulk value [Bowers] therefore larger than the thermal conductivity measured for InSb NWs in Reference [Zhou]. This could be due to the clean crystalline structure of the investigated NWs, together with the fact that in the investigated NWs diameter range a strong effect of boundary scattering is not expected since the phonon mean free path at 300 K is ~84 nm [Seol]. The fitted value for κ_{air} ranges from 0.09 to 0.18 W/mK (data not shown) and it is, therefore, much smaller than the NW thermal conductivities.

In Figure 3(d) we show the parameter values calculated from the fitting for the thermal contact resistances at source and drain $R^{\mathrm{C}}_{\mathrm{S,D}}$. For each NW we obtain $R^{\mathrm{C}}_{\mathrm{S}} \neq R^{\mathrm{C}}_{\mathrm{D}}$, that explains the asymmetric shape of the Raman temperature profiles (see Figure 2(b)). It is important to note that the NW thermal resistances are ~3 to 40 times larger than the contact thermal resistances, which thus have a minor effect. More interestingly, the obtained values are ~2 orders of magnitude lower than the measured thermal contact resistances for similar nanostructures on SiN_x membranes [Zhou2011a]. This is clearly an important advantage of the method here described, and the large difference is likely due to the fact that more standard and reliable contacting procedures can be used in our case.

In order to further prove the reliability of the presented method, we present the results of Seebeck coefficient and electrical conductivity determined by all electrical field-effect measurements on the same Se-doped InSb NW as-grown sample investigated with the combined Raman-transport method.

5. S and σ determined by field-effect transistor measurements

Since the excitation laser has energy far above the InSb bandgap, one issue that needs to be considered is the presence of other possible mechanisms that can generate current in semiconductors exposed to illumination. Spatially resolved photocurrent measurements have been extensively used to investigate carrier transport in NWs, nanotubes and thin films [Pettersson, Thunich, Varghese, Prechtel2012, Ehrard, St-Antoine2009, St-Antoine2012, Prechtel2011, Prechtel2012a, Buscema]. In addition to thermoelectric effect, light exposure can generate built-in electric field responsible for electron-hole separation, which can diffuse or drift to the electric contacts. Recently, electro-thermodynamic modeling of semiconductor NWs under local injection of non-equilibrium carriers has shown the interplay of the different effects, and predicted photocurrent profiles for different types of electrical contacts [Fu]. Time-resolved scanning photocurrent measurements on GaAs and InAs NWs, carbon nanotubes, and graphene have been used to resolve the different temporal contributions to the photocurrent at the picosecond time scale [Prechtel2012, Ehrard, Prechtel2011, Prechtel2012a].

In order to understand the role of possible photo-excited charge carriers, independent field-effect transistor measurements of electrical conductivity and Seebeck coefficient of individual InSb NWs were performed, indicating consistent findings with the results from the combined Raman spectroscopy and transport measurements. This is a strong evidence that, even if present, the photovoltaic effect in our measurements is negligible with respect to thermal effects. Furthermore, the temperature dependence of the electrical conductivity as measured from all-electrical measurements

(shown in Figure S8) is comparable with the behavior observed with combined Raman and electrical measurements method (Figure 2(c)), indicating that thermal effects are prevalent in the system.

Figure 4(a) shows one of the NW field-effect transistors (FETs) devices. Se-doped InSb NWs were drop-casted over a SiO_2/Si substrate and source and drain electrodes were fabricated at a relative distance of 1.1 μm. The multicontact arrangement visible in figure allows to operate the electrodes both as electrical leads and resistive thermometers, sampling temperatures T_S and T_D at the two ends of the FET and the thermal bias $\Delta T = T_D - T_S$. Operation details and performance of the heating scheme, together with precise information on the measurement procedure, have been presented elsewhere [RodNL2013,RodNR2014]. The direct measurement of T_D and T_S, together with the large ΔT attainable, allow us to determine the precise mapping of $S(\sigma,T)$ in the explored temperature range for ΔT ranging from a minimum of ≈0.6 K to a maximum of ≈8.5 K. Figure 4(b) report the S *vs* σ curves obtained for five different temperatures above 300 K. The device was thermalized at temperature of 295 K, then the local heater was voltage biased so to establish along the NW the temperature difference indicated in parenthesis in Figure 4(b). S exhibits a monotonic dependence on T for every given value of σ, and the T-dependence of S is linear in first approximation (although this is more evident in the S/T *vs* σ curves reported in the Supplementary Information). The corresponding power factor $S^2\sigma$ is plotted as function of σ in Figure 4(c).

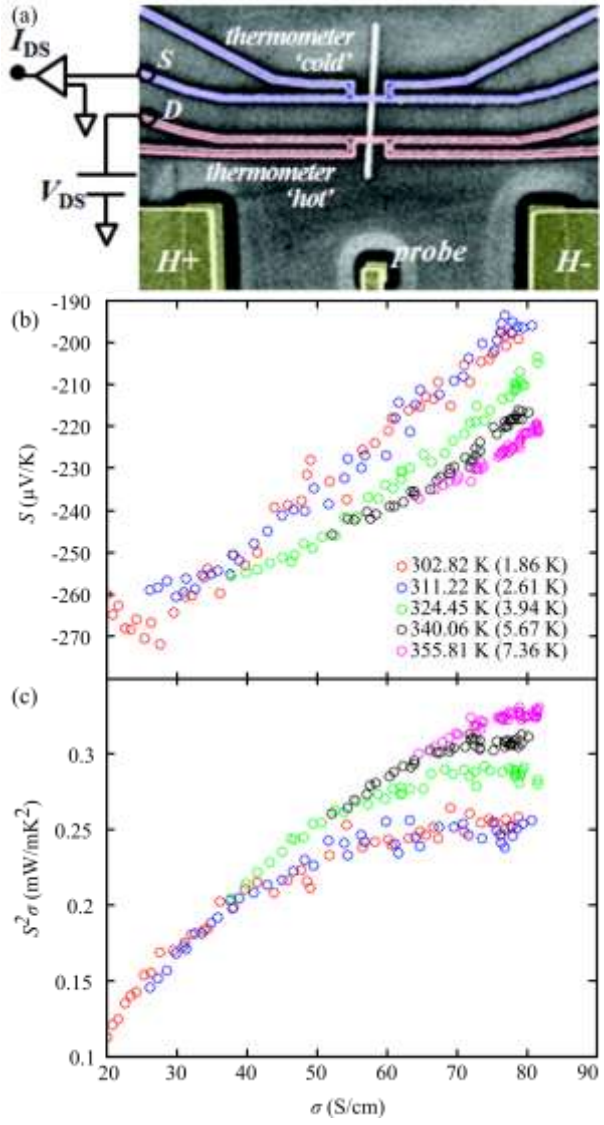

Figure 4. Field-effect Seebeck measurements of individual InSb NWs. (a) Scanning electron micrograph of one of the investigated devices. The NW is deposited onto a 300 nm SiO_2 layer grown

on top of n-doped bulk silicon substrate, which acts as a back-gate. A buried heater (*H*+, *H*-) is adopted to induce temperature gradients up to 8 K/μm along the NW axis. Four-terminals Ti/Au electrodes are fabricated at the hot and cold sides of the nanostructure, allowing the AC electrical detection of the temperature difference established between the NW ends and, simultaneously, the DC measurement of the *I-V* characteristic. The measurement set-up, whose DC part is sketched in the overlay, allows the field-effect control of the resistance *R* and of the Seebeck coefficient *S*. (b) *S* as a function of the electrical conductivity σ at different temperatures above 300 K. The corresponding temperature differences between the hot and cold end of the NW are reported in brackets. The values of *S* are extracted by the measurement of *R* and of the thermovoltage V_{th} for applied back-gate voltages in the range (0,+10 V). (c) Power factor $S^2\sigma$ as a function of σ at different temperatures.

We highlight that the results obtained using the two different methods very nicely match. In both cases we have measured individual InSb NWs with diameters around 180 nm coming from the same growth batch. From the comparison of the data reported in Figure 3 and Figure 4(b)-(c), the emerging scenario is that NWs exhibit Seebeck coefficient *S* in the range 150-250 μV/K for temperatures above 300 K, while the power factor $S^2\sigma$ exceeds 0.3 with σ > 8 kS/m.

We also aimed to separate the temporal contribution of the thermocurrent and photocurrent *via* frequency dependent measurements modulating the laser with an optical chopper. The chopper frequency dependent measurements are shown in the SI9 (Figure S14). We observed a significant variation on the measured photocurrent starting from ~3 kHz chopping frequency up to ~6 kHz, depending on the laser position along the NW. This means that the main contribution to the photocurrent is due to mechanism happening in the time scale of ~300 μs. Since photocurrent is expected to have a shorter time scale than thermal mechanism [St-Antoine2012], we believe that the measured current is driven by thermal effects.

6. ZT analysis

From the fitting of the electrical data and of the temperature profiles, we could estimate the thermal conductivity κ and the Seebeck coefficient *S* of our InSb NWs. The two quantities together with the electrical conductivity measured from the *I-V* characteristic curves provide the thermoelectric figure of merit *ZT*. We extracted the *ZT* value at zero power from the power dependence of the maximum *ZT* measured along the NWs. Details of the figure of merit calculation are described in the SI.

The results we obtained for the investigated NWs are summarized in Figure 5.

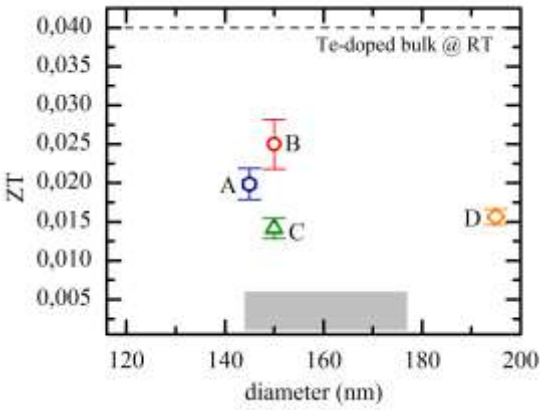

Figure 5: Figure of merit ZT for the Se-doped InSb NWs at zero laser power. Each symbol indicates a different NW. The ZT bulk single crystal value for Te-doped InSb is marked as a dashed line and the range of values obtained by NWs from ref. [Zhou] is marked as shadowed grey area.

Together with our results, we show the *ZT* value obtained for Te-doped InSb bulk single crystal at room temperature [Yamaguchi] as a dashed line, and the range of values measured for two Sb-doped InSb NWs from Ref. [Zhou] marked as shadowed grey area. For Se-doped InSb NWs with diameters between 130 and 195 nm we find *ZT* values between 0.014 and 0.025 at room temperature. These values are larger than the values reported for Sb-doped InSb NWs, with similar diameters [Zhou]. The larger Seebeck coefficients compensate the smaller suppression of the thermal conductivity with respect to reference [Zhou]. We can attribute this enhancement of *ZT* to a higher electronic mobility with respect to reference [Zhou].

Conclusion

In conclusion, we showed a new method for the complete thermoelectric characterization of single semiconductor NWs, and we applied it to Se-doped InSb NWs. Combined laser heating, Raman spectroscopy and simple electrical measurements allow the determination of the NW thermoelectric figure of merit *ZT*, together with the estimate of the thermal contact resistances at the nanowire-source/drain contacts. The temperature and electrical data are well described by 1D heating model which includes Gaussian heat source. Device fabrication consists in standard litography techniques, and it is therefore relatively simple. Comparison with field-effect transistor Seebeck measurements shows a good agreement between the obtained results, demonstrating the validity of the method.

The *ZT* of Se-InSb ranges between 0.014 and 0.025 at room temperature, the highest *ZT* measured in InSb nanowires to the best of our knowledge.

Acknowledgements

We thank M Bichler and H Riedl for excellent experimental help. We acknowledge financial support by the Deutsche Forschungsgemeinschaft via the Excelence Cluster “Nanosytems Initiative Munich” and the TUM Institute for Advanced Study. F.R. acknowledges financial support from the Italian MIUR through the FIRB - “Futuro in Ricerca” project BFR13NEA4 “UltraNano”.

References

[Hicks1] Hicks, L. D.; Dresselhaus, M. S. *Phys. Rev. B* **1993**, *47*, 12727-12731.

[Hicks2] Hicks, L. D.; Dresselhaus, M. S. *Phys. Rev. B* **1993**, *47*, 16631-16634.

[Majumdar] Majumdar, A. *Science* **2004**, *303*, 777-778.

[Heremans] Heremans, J. P.; Dresselhaus, M. S.; Bell, L.E.; Morelli, D. T. *Nature Nanotechnology* **2013**, *8*, 471-473.

[Zhao] Zhao, L.-D.; Lo, S.-H.; Zhang, Y.; Sun, H.; Tan, G.; Uher, C.; Wolverton, C.; Dravid V. P. & Kanatzidis M. G. *Nature* **2014**, *508*, 373-378.

[Roh] Roh, J. W.; Jang S. Y.; Kang, j.; Lee, S.; Noh, J.-S.; Kim, W.; Park, J.; Lee, W. *Apll. Phys. Lett.* **2010**, *96*, 103101.

[Li] Li, D.; Wu, Y.; Kim, P.; Shi, L.; Yang, P.; Majumdar, A. *Apll. Phys. Lett.* **2003**, *83* 2934.

[Zhou2011] Zhou, F.; Moore, A. L.; Bolinsson, J.; Persson, A.; Froeberg, L.; Pettes, M. T.; Kong, H.; Rabenberg, L.; Caroff, P.; Stewart, D. A.; Mingo, N.; Dick, K. A.; Samuelson, L.; Linke, H.; Shi, L. *Phys. Rev. B* **2011**, *83*, 205416.

[Doerk2010] Doerk, G. S.; Carraro, C.; Maboudian, R. *ACS Nano*, **2010**, *4*, 4908–4914

[Soini] Soini, M.; Zardo, I.; Uccelli, E.; Funk, S.; Koblmüller, G.; Fontcuberta i Morral, A.; Abstreiter, G. *Appl. Phys. Lett.* **2010,** *97*, 263107.

[Zhou2006] Zhou, F.; Seol, J. H.; Shi, L.; Ye, Q. L.; Scheffler, R. *J. Phys.: Condens. Matter* **2006**, *18*, 9651-9657.

[Shapira] Shapira, E.; Tsukernik, A.; Selzer, Y. Nanotechnology 2007, 18, 485703.

[RodNL2013] Roddaro, S.; Ercolani, D.; Mian, A.; Suomalainen, S.; Rossella, F.; Giazotto, F.; Sorba, L.; Beltram, F., Nano Lett. 2013, 13, 3638−3642.

[Shi2003] Shi, L.; Li, D. Y.; Yu, C. H.; Jang, W. Y.; Kim, D.; Yao, Z.; Kim, P.; Majumdar, A. *Journal of Heat Transfer*, **2003**, *125*, 881–888.

[Shi2012] Shi, L. *Nanosc. Miscrosc. Therm.* **2012**, *16*, 79-116.

[Zhou2011a] Zhou, F.; Perrson, A.; Samuelson, L.; Linke, H.; Shi, L. *Appl. Phys. Lett.* **2011**, *99*, 063110.

[Mingo] Mingo, N. *Appl. Phys. Lett.* **2004**, *84*, 2652.

[Stuckes] Stuckes, A. D. *Phys. Rev.* **1957**, *107*, 427-428.

[Bowers] Bowers, R.; Ure Jr., R. W.; Bauerle, J. E.; Cornish, A. J. *J. Appl. Phys.* **1959**, *30*, 930-934.

[Mielczarek] Mielczarek, E. V.; Frederiske, H. P. R. *Phys. Rev.* **1959**, *115*, 888-891.

[Busch] Busch, G.; Steigmeier, E. *Helv. Phys. Acta*. **1961**, *34*, 1-28.

[Holland] Holland, M. G. *Phys. Rev.* **1964**, *134*, A471-A480.

[Bhandari] Bhandari, C. M.; Verma, G. S. *Phys. Rev.* **1965**, *140*, A2101-A2104.

[Kosarev] Kosarev, V. V.; Tamarin, P.V.; Shalyt, S. S. *Phys. Stat. Solidi (b)* **1971**, *44*, 525-530.

[Nakwaski] Nakwaski, W. *J. Appl. Phys.* **1988**, *64*, 159.

[Yamaguchi] Yamaguchi, S.; Matsumoto, T.; Yamazaki, J.; Kaiwa, N.; Yamamoto, A. *Appl. Phys. Lett.* **2005**, *87*, 201902.

[Zhou] Zhou, F.; Moore, A. L.; Pettes, M. T.; Lee, Y.; Seol, J. H.; Ye, Q. L.; Rabenberg, L.; Shi, L. *J. Phys. D: Appl. Phys.* **2010**, *43*, 025406.

[Carles] Carles, R.; Landa, .; Renucci, J.B. Solid State Communications, 1985, 53, 179.

[Costa] Costa, S. C.; Pizani, P. S.; Rino, J. P. Phys. Rev. B 2003, 68, 073204.

[Zardo] Zardo, I.; Conesa-Boj, S.; Peiro, F.; Morante, J. R.; Arbiol, J.; Uccelli, E.; Abstreiter, G.; Fontcuberta i Morral, A. Phys. Rev. B 2009, 80, 245324.

[Liarokapis] Liarokapis, E.; Anastassakis, E. Phys. Rev. B 1984, 30, 2270(R).

[Yazji] Yazji, S.; Zardo, I.; Soini, M.; Postorino, P,; Fontcuberta i Morral, A.; Abstreiter, G. Nanotechnology 2011, 22, 325701

[Doerk2009] Doerk, G. S.; Carraro, C.; Maboudian, R. *Phys. Rev. B* **2009**, *80*, 073306.[Ahn] Ahn, Y.; Dunning, J.; Park, J. *Nano Lett.*, **2005**, *5*, 1367.

[Oskooi] Oskooi, A. F.;Roundy, D.; Ibanescu, M.; Bermel, P.; Joannopoulos, J.D.; Johnson, S.G. Comp. Phys. Commun. 2010, 181, 687-702.

[Seol] Seol, J.H. Thermal and thermoelectric measurements of silicon nanoconstrictions, supported graphene, and indium antimonide nanowire. PhD Thesis, UT *Electronic Theses* and *Dissertation.*

[Pettersson] Pettersson, H.; Tragardh, J.; Persson, A. I.; Landin, L.; Hessman, D.; Samuelson, L. *Nano Lett*. **2006**, 6, 229.

[Thunich] Thunich, S.; Prechtel, L.; Spirkoska, D.; Abstreiter, G.; Fontcuberta i Morral, A.; Holleitner, A. W. *Appl. Phys. Lett.* **2009**, *95*, 083111.

[Varghese] Varghese, B.; Tamang, R.; Tok, E. S.; Mhaisalkar, S. G.; Sow, C. H. *J. Phys. Chem. C* **2012**, 114, 15149.

[Prechtel2012] Prechtel, L.; Padilla, M.; Erhard, N.; Karl, H.; Abstreiter, G.; Fontcuberta i Morral, A.; Holleitner, A. W. *Nano Lett.* **2012**, *12*, 2337.

[Ehrard] Erhard, N.; Seifert, P.; Prechtel, L; Hertenberger, S.; Karl, H.; Abstreiter, G.; Koblmüller, G.; Holleitner, A. W. *Ann. Phys. (Berlin)* **2013**, *525*, 180.

[St-Antoine2009] St-Antoine, B. C.; Ménard, D.; Martel, R. *Nano Lett.* **2009**, *9*, 3503.

[St-Antoine2012] St-Antoine, B. C.; Ménard, D.; Martel, R. *Nano Res.*. **2012**, *5*, 73.

[Prechtel2011] Prechtel, L.; Song, L.; Manus, S.; Schuh, D.; Wegscheider, W.; Holleitner, A. W. *Nano Lett*. **2011**, 11, 269.

[Prechtel2012a] Prechtel, L.; Song, L.; Schuh, D.; Ajayan, P.; Wegscheider, W.; Holleitner, A. W. *Nat. Commun.* **2012**, *3*, 646.

[Buscema] Buscema, M.; Barkelid, M.; Zwiller, V.; van der Zant, H. S. J.; Steele, G. A.; Castellanos-Gomez, A. *Nano Lett.* **2013**, *13*, 358.

[Fu] Fu, D.; Zou, J.; Wang, K.; Zhang, R.; Yu, D.; Wu, J. *Nano Lett.* **2011**, *11*, 3809.

[RodNR2014] Roddaro, S.; Ercolani, D.; Mian, A. S.; Rossella, F.; Piazza, V.; Giazotto, F.; Sorba, L.; Beltram, F., Nano Research 2014, 7, 579-587.